Fully implantable optoelectronic systems for battery-free, multimodal operation in neuroscience research

Philipp Gutruf [1,2], Vaishnavi Krishnamurthi[3], Abraham Vázquez-Guardado [4,5], Zhaoqian Xie[6], Anthony Banks[7], Chun-Ju Su[1], Yeshou Xu[8], Chad R. Haney[9], Emily A. Waters [10], Irawati Kandela[11], Siddharth R. Krishnan[1], Tyler Ray [1], John P. Leshock[12], Yonggang Huang[6], Debashis Chanda[4,5] and John A. Rogers [13]*

Recently developed ultrasmall, fully implantable devices for optogenetic neuromodulation eliminate the physical tethers associated with conventional set-ups and avoid the bulky head-stages and batteries found in alternative wireless technologies. The resulting systems allow behavioural studies without motion constraints and enable experiments in a range of environments and contexts, such as social interactions. However, these devices are purely passive in their electronic design, thereby precluding any form of active control or programmability; independent operation of multiple devices, or of multiple active components in a single device, is, in particular, impossible. Here we report optoelectronic systems that, through developments in integrated circuit and antenna design, provide low-power operation, and position- and angle-independent wireless power harvesting, with full user-programmability over individual devices and collections of them. Furthermore, these integrated platforms have sizes and weights that are not significantly larger than those of previous, passive systems. Our results qualitatively expand options in output stabilization, intensity control and multimodal operation, with broad potential applications in neuroscience research and, in particular, the precise dissection of neural circuit function during unconstrained behavioural studies.

The discovery of microbial opsins and their application in neuroscience research provides a basis for activating targeted neurons by optical means[1], and led to a new set of methodologies for neuroscience research, known collectively as optogenetics[2]. Broad applications of optogenetics now exist through the activation and inhibition of selected behaviour centres in the brain and the peripheral nervous system[3]. The delivery of light at appropriate intensities to tissues of interest is critically important to optogenetic studies[4]. The simplest and most common methods involve optical fibres[5] that are physically tethered to external light sources, but this type of mechanical and optical interface leads to damage to the surrounding tissue and optical attenuation[6]. The tethers also affect behaviours and can frustrate experimental efforts to decipher mechanisms and functions of the brain. Recently introduced wireless, miniaturized subdermal platforms for delivering light in a battery-free mode of operation provide key advantages by minimizing micro-motions and therefore scar formation at the probe interface. They also enable unconstrained, tether-free operation. This capability allows for experimental test set-ups and protocols

without the need for advanced habituation and handling of the animals[7]. Operation in a range of environments and contexts is also possible, including social interactions, that would otherwise be difficult to explore.

Although the latest examples of such tools require only simple electronics, they do not offer precise control over the light intensity and they cannot support multimodal operation or independent control over multiple devices[8]. Instead, operation involves external modulation of the source of radiofrequency power, such that the devices themselves require only passive components[9]. Shaping the field intensity to achieve a uniform distribution across a region of interest usually comes at the expense of antenna complexity (requiring, for example, resonant cavities and antenna arrays[10]), which becomes more difficult with increasing experimental area and layout intricacy. The very latest approaches involve magnetic resonant coupling and loop antennas, with variations of 30–50% in typical experimental cages, which is sufficient for many experiments[7,10,11]. However, precise regulation and programming of the output intensity may be necessary in certain demanding cases, such as those

that require activation of two distinct opsins[12] or those that involve challenges in the avoidance of photobleaching[13]. New experimental approaches that require spatial control over multiple illumination sites with dense optical stimulation in a given subject are also important in studies of cellular-level interactions of neurons, such as phase precession generation[14], and have been shown only in restrained or tethered animals. Furthermore, on a macro scale, bilateral stimulation that targets distinct brain regions to reveal circuit-level interactions is desirable[15]. In this Article, we report the development of implantable optoelectronic systems that address these requirements directly, and without noticeably increasing the weight or size, or the basic wireless, battery-free operation of current passive platforms. Our use of commercially available electronics and manufacturing schemes offers immediate opportunities for broad distribution in the neuroscience community.

Active power regulation and digital control for optogenetics

Despite their limitations, tethered optogenetic approaches have the advantage of consistent power output as the animal navigates its environment. This level of signal continuity must be matched by wireless platforms. The strategy for providing precise control over the optical intensity builds on the platform presented in Shin and colleagues[7], which uses magnetic resonant coupling for efficient power transfer with minimal device size, component count and weight. In this work we introduce active electronic circuits without increasing the size or volume of the circuitry substantially, to yield a mechanically robust and overall thin, flexible form factor that is critically important for successful deployment as a subdermal implant. Figure 1 shows the physical and electrical designs of three advanced devices with these essential features, but configured for optically stable optogenetic stimulation/inhibition in small animal subjects, such as mice, with full control over illumination intensity and spatial location.

Figure 1a provides an exploded-view schematic illustration of a device that guarantees that optical output remains at a defined value, when operational, regardless of position or orientation within an experimental enclosure. This device uses an active, feedback-regulated constant voltage supply to an implantable microscale inorganic light emitting diode (μ-ILED, from a commercial vendor) that serves as the light source for optogenetic modulation. The design features an extendable, articulated implantable needle, as previously reported (Supplementary Fig. 1a) for facile positioning in the brain, together with a flexible electronics platform that can be affixed to the surface of the skull in a subdermal fashion. The electrical layout is shown in Fig. 1b. The system consists of a purpose-designed rectifier made of specialized, radiofrequency (RF) Schottky diodes and a linear dropout regulator (LDO). The power delivered to the implanted μ-ILED, and to a separate, subdermal red indicator μ-ILED, can be adjusted by selecting the current limiting resistors R1 and R2.

Figure 1c shows the makeup of a multimodal device that is capable of optogenetically modulating neuron activity in four spatially distinct sites with programmable frequency and duty cycle. Here, two separately injectable filaments support two μ-ILEDs each, with detailed dimensions in Supplementary Fig. 1b. The electrical design, shown in Fig. 1d, involves a minimal component count. The rectification and power regulation components are identical to those described above. An additional microcontroller provides timing and illumination control over the μ-ILEDs. Control over the stimulation parameters follows from a custom protocol that relies solely on amplitude modulation of the RF that simultaneously powers the implant and is user adjustable in real time.

Finally, Fig. 1e shows a device that features programmable control over the intensity. The design in Fig. 1f involves the same building blocks, including a microcontroller, as for the multimodal device, but also integrates a digital-to-analogue converter (DAC)

made up of a second-order lowpass filter and an operational amplifier in a voltage-follower configuration to decouple the μ-ILED load from the lowpass filter, as shown in the red dashed box in Fig. 1f. Here, the added complexity and component count of such a DAC provides non-pulsewidth-modulated output, which can lead to false results with the newest generation of fast opsins, such as Chronos[16]. This DAC can provide output frequencies up to 1.5 kHz, well above the response speeds of current opsins, with full control over the optical output intensity. Photographic images of these device types, each balanced on a fingertip, are shown in Fig. 1g–i and injectable dimensions are shown in Supplementary Fig. 1c. These images also highlight the thin, flexible form factors that facilitate subdermal implantation.

Spatially independent operation across large assays

Critical to the successful operation of all of these devices are designs that efficiently harvest RF power provided via magnetic resonant coupling in common behavioural environments. Figure 2 shows the electrical characterization of the rectifier and the active regulation that enables constant power delivery to the μ-ILEDs. Power delivery to the implant occurs by a single wave rectifier that consists of a matching capacitor for tuning the system to an operational frequency of 13.56 MHz and two Schottky diodes with low forward-voltage thresholds for rectifying the AC signal such that passage through a smoothing capacitor (2.2 μF) produces a stable DC voltage. The two-diode set-up isolates the RF from the DC side to reduce noise and stabilize the analogue and digital circuits. The low internal capacitance of these diodes (0.2 pF) at 13.56 MHz minimizes losses in the rectifier. Additional benefits include isolation of the resonant circuit from the digital electronics. Figure 2a shows the rectification behaviour with decreasing Ohmic loads. The peak rectified power occurs at a rectified voltage of 2.5–3.5 V, with steep reductions for voltages below 2.5 V. Operation with a stable rectification voltage of 2.8–3.3 V allows for high power extraction. The sharp drop-off in rectified power at higher loads can be explained by the Q-factor of the coil, shown in Supplementary Fig. 2i. Specifically, the Q-factor decreases with increasing load, thereby reducing the coupling efficiency between the primary and secondary antenna.

The available electrical power from the rectifier with a conventional dual loop antenna in standard experimental set-ups can be measured with a shunt resistor (5.6 kΩ) as a function of input power to a dual loop primary antenna that circumflexes the experimental area (dimensions of the loop are shown in Supplementary Fig. 2a,b). The resulting power distribution scales with the input power, where the available power increases with input power while the relative spatial power distribution (uniformity) remains constant, as illustrated in Supplementary Fig. 2c for the case of 4 W of input power and in Supplementary Fig. 2d for 8 W in the case of a standard experimental arena (30 cm × 30 cm). The data also reveal that the size of the enclosure determines the power available at the implant; a mouse home cage, which is about half the area studied here, shows significantly improved power and uniformity (Supplementary Fig. 2e,f). The uniformity involves a drop of approximately 50% in the centre of the enclosure, which translates directly into a decrease in optical power, as shown in Supplementary Fig. 2g, as determined by the electrical to optical power conversion, shown in Supplementary Fig. 2h, of an unregulated device as comparison. These results are consistent with the uniformity previously reported in the literature[7].

Power at the implant also depends on the relative angle to the primary coil, with sharp decreases as this angle increases above a certain threshold (Supplementary Fig. 3a). Such behaviour can be problematic for certain postures of the animal as it actively explores its environment, particularly problematic for animals that move in three-dimensional (3D) space, such as fish[17] and birds[18]. Here, an angle-independent supply of wireless power becomes a critical
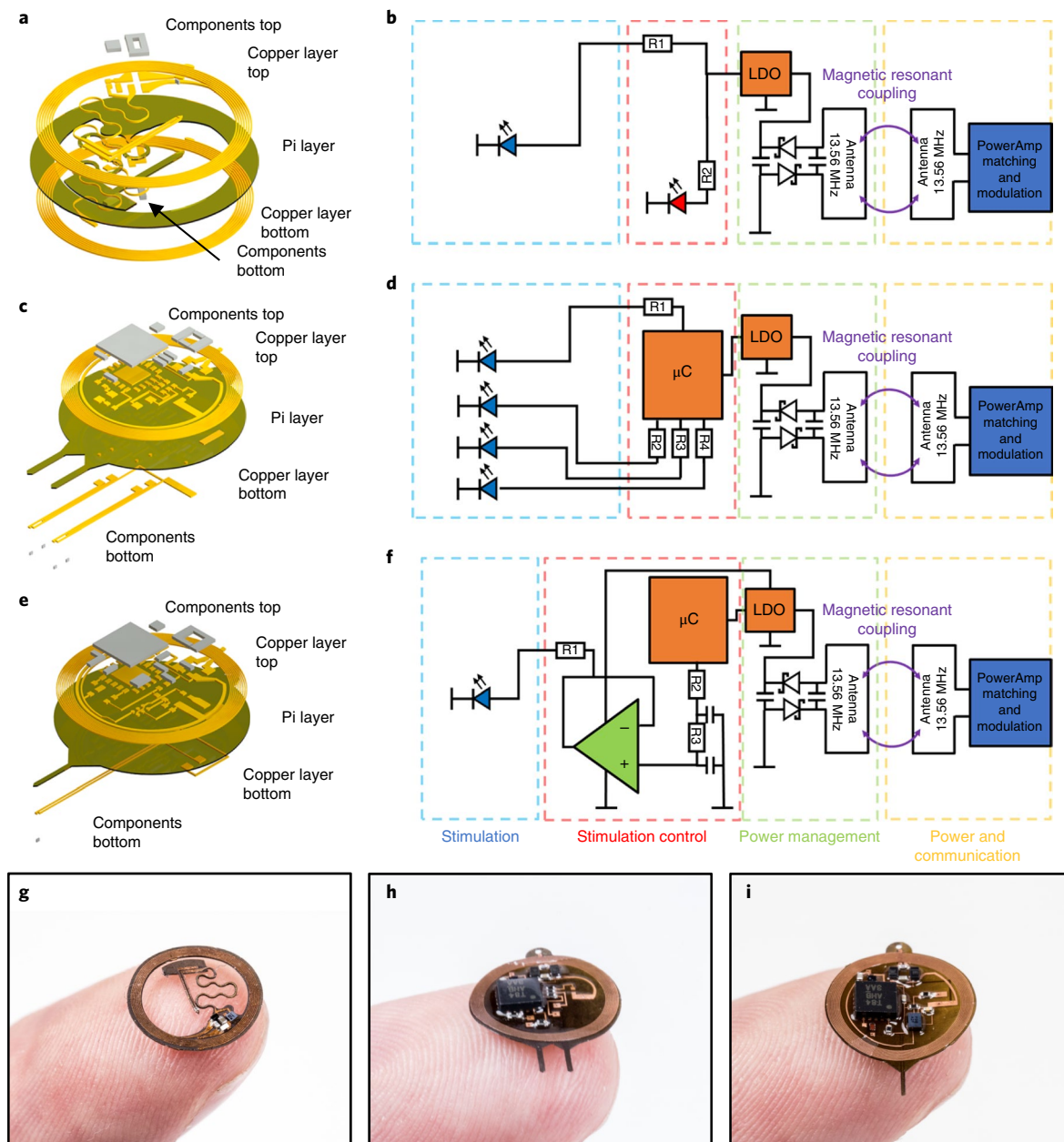
Fig. 1 | Digitally controlled multimodal optogenetic implants. a,b, Layered view (**a**) and electrical schematic (**b**) of a power regulated system with minimal footprint. **c,d,** Layered view (**c**) and electrical schematic (**d**) of an advanced bilateral system with four individually controlled light sources in a multi μ-ILED device. **e,f,** Layered view (**e**) and electrical schematic (**f**) of the programmable intensity device. Electrical components for panels **b**, **d** and **f**: blue LED symbol, μ-ILED; red LED symbol, red indicator LED; Schottky diode symbol, RF Schottky diode; capacitor symbols, ceramic capacitors. **g,** Photographic image of the regulated implantable device. **h,** Photographic image of the programmable multi μ-ILED device. **i,** Photographic image of the programmable intensity device.

aspect of system design for many behavioural paradigms. To mitigate angle-dependent power transmission, we demonstrate a system that combines two resonant magnetic antennas that produce predominantly orthogonal fields, thereby supporting angle-independent powering of implants. The antenna system shown in Fig. 2b consists of antenna 1, which produces a vertical field, and antenna 2, which produces a horizontal field, as shown in the finite-element simulations. The antennas are rapidly multiplexed (5 kHz) to produce a DC power supply, independent of the angular orientation, after passing through the rectifier on the implant. Resulting measurements of the power distribution of such an active antenna system show correlated field variations in space and angle, as shown in

Fig. 2c at a physiologically relevant height of 6 cm, which represents an average height of the cage floor for mice (mice on front paws 3 cm off ground and on hindlegs 9 cm off ground). Power levels remain sufficiently high irrespective of angle and position in the cage, as verified in Supplementary Fig. 3b–d with measurements and corresponding simulation results, to enable operation of devices capable of producing optogenetic stimulus.

The active regulation system summarized in Fig. 1b eliminates variations in power harvesting. In particular, the direct feedback provided by the electronics guarantees an output fixed to a predetermined voltage, thereby yielding a binary operation, that is 'ON' to a set value if the RF power is sufficient and 'OFF' if it is not.
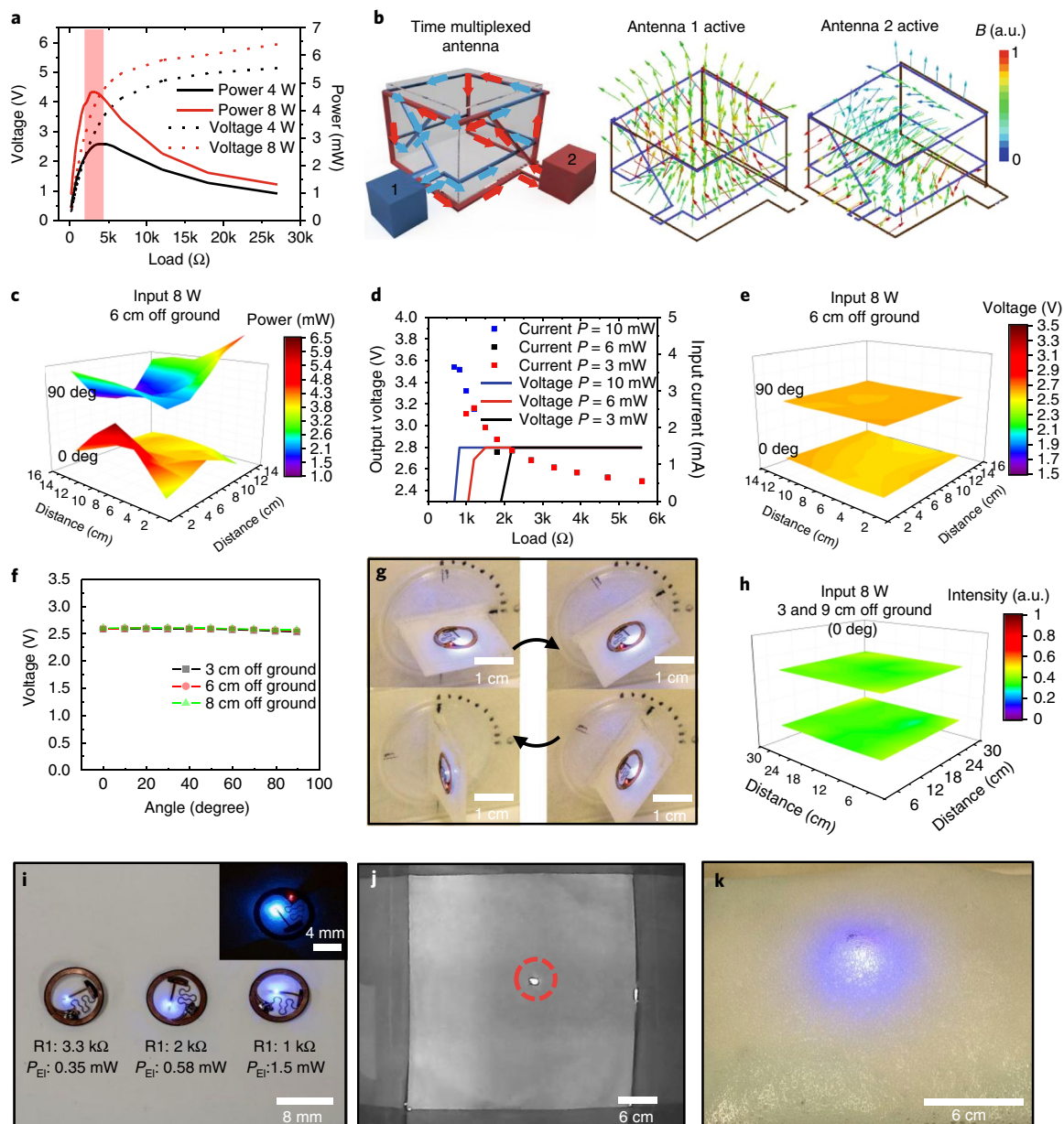
Fig. 2 | Electronic and optical characterization. a, Measurement of rectifier voltage and power with increasing load placed in the centre of a field created by a 15 cm × 30 cm cage with 4 W and 8 W primary antenna power. **b**, Schematic illustration (left) of a time-multiplexed antenna system designed to eliminate any angle and position dependence of the operation of the implant. The renders on the right show the results of finite-element modelling the resulting magnetic field distribution (*B*) for each of the two antennas. **c**, Rectified power at the implant measured with 8 W input power applied to a time-multiplexed antenna across a cage (20 cm × 20 cm) at an implant height of 6 cm and at orientations of 0 and 90 degrees with respect to ground. **d**, Regulated output voltage and supply current with three power levels (*P*) measured at decreasing load, demonstrating the dropout behaviour of the regulator. **e**, Regulated voltage at the implant measured with 8 W input power in a time-multiplexed cage (20 cm × 20 cm) at an implant height of 6 cm and at orientations of 0 and 90 degree with respect to ground. **f**, Measurement of the regulated voltage using a µ-ILED for stimulation and an indicator LED load with 3.3 kΩ and 5.6 kΩ current-limiting resistors, respectively, at heights of 3, 6 and 8 cm above ground with increasing angle, demonstrating stable output throughout angle and space. **g**, Photographic images of a regulated implant with increasing angle in a time-multiplexed cage using a current-limiting resistor on the stimulator (3.3 kΩ) µ-ILED and indicator (5.6 kΩ) LED. **h**, Optical output intensity of a regulated implant at 3 and 9 cm height in a single primary antenna (power 8 W in a 30 cm × 30 cm cage). a.u., arbitrary units. **i**, Devices with various power settings for the µ-ILED demonstrating versatility of circuit layout. The inset shows an option with a red indicator LED. **j**, Photographic image with an infrared sensitive camera in darkness, demonstrating the infrared indicator light for tracking purposes. **k**, Photographic image of a regulated device operating submerged in optically and acoustically attenuating aqueous foam.

The behaviour with increasing load is shown in Fig. 2d. The output voltage is stable until the connected load exceeds the input power capability. The resulting drop in voltage is linear and rapid, which results in the device either performing at the specified power level or not operating at all. The switching performance across a range of commonly used frequencies in optogenetics is shown in Supplementary Fig. 3e. Above the dropout voltage of 150 mV, at an input voltage of 3 V with a regulated output voltage of 2.8 V, the efficiency of the regulator is approximately 85%, independent of load. The regulator also has the additional benefit that the rectifier

voltage remains in its optimal range of 2.5–3.5 V regardless of the load. This feature is especially beneficial for μ-ILEDs with low turn-on voltages, as it greatly increases system efficiencies in comparison to designs that involve directly connected μ-ILEDs. Figure 2e shows the output voltage with an μ-ILED load and the current-limiting resistor R1 set to 3.3 kΩ. The results indicate a stable output voltage regardless of the orientation and position of the implant, with 0.1% output variation when powered by a primary antenna input of 8 W with a multiplexed antenna system (5 kHz). The operation of a device oriented at increasing angles normal to the loop antenna 1 is shown in Fig. 2f, where the device with load (μ-ILED and R1 3.3kΩ) is tilted from 0 to 90 degrees at various heights in the cage. Here we observe stable voltage regardless of position and angle. A visual representation of the experiment is shown in Fig. 2g. This performance is noticeably improved over that of a non-multiplexed system; see Supplementary Fig. 3f. Measurements that illustrate the expected, stable optical output across the experimental area appear in Fig. 2h, here performed with a 0 degrees implant orientation using an automated imaging technique. Optical output power variations realized by setting resistor R1 are shown in Fig. 2i. Operation of two immediately adjacent devices orthogonally oriented is also possible, as shown in Supplementary Fig. 3h,i, which has important applications for simultaneous operation of multiple devices in a single animal model. A stable electrical output also allows integration of indicator μ-ILEDs that reside subdermally such that their output can be visually observed through the skin/fur. Red (Fig. 2i inset) LEDs are of interest because rodents have exceptionally low perception in this range of wavelength. Infrared μ-ILEDs represent another option (Fig. 2j) of interest for automated tracking, due to the high contrast against visible wavelengths. In both cases, the intensity can be tuned via the current-limiting resistor R2, and can therefore be balanced, as desired, with the current available for the optogenetic μ-ILEDs. In a typical set-up, the indicator μ-ILEDs operate at much smaller powers (usually well below 1 mW) than the optogenetic μ-ILEDs, simply because the red and infrared light can be detected easily through the skin/fur, even at very low intensities.

Digital control over patterns of optical stimuli

Another advantage of this technology is the low absorption of power at the operational frequency (13.56 MHz). Attenuating tissues and structures found in the body, such as optically and acoustically scattering media, can prohibit the use of other wireless power-harvesting schemes based on optics and acoustics, especially in larger animal models. The devices presented here are unaffected by such media, and can operate through optically, acoustically and high-frequency attenuating media, as shown in Fig. 2k, where an active device operates inside an aqueous foam matrix and through large bodies of water (Supplementary Fig. 3j). Multimodal operation, in terms of independent control over the intensity of multiple μ-ILEDs, can also be useful. Such features require wireless communication with the implant, which is challenging due to high power requirements for operating the μ-ILEDs and the limited power availability, especially in large experimental environments. Commercial near-field communication (NFC) technologies involve antenna systems specifically designed to support modulation methods for communication, which result in antenna and matching circuits that must have bandwidths of at least 1 MHz. This requirement demands low Q factors for the antennas and, consequently, inefficient power transfer capabilities for receiver antennas that are sufficiently small for implantation in animal models such as mice. A method for one-way communication introduced here circumvents these problems. Figure 3a describes the functionality of the system, where the non-volatile memory of a microcontroller stores program states, and modulation in the primary antenna power serves to trigger these stored states. The program states can include all desired

experimental protocols for the implant. A schematic description appears in Fig. 3b.

A modulation scheme that allows the user to switch between program states, as inspired by one-wire data connections where the ON time on the bus determines a logical 0 or 1, is shown in Fig. 3b. The beginning of a data flag is triggered by a specific ON time (t_1) that initiates communication. Program states are then triggered with subsequent primary power pulses with different ON times (t_2). The hardware requirement for this protocol is minimal, as the only facilities needed in the microcontroller are a non-volatile memory and a set of timers. The result affords a high degree of design freedom, without the use of application-specific integrated circuits (ASICs) or other complex electronics and commercially available schemes, such as NFC integrated system on a chip, which have major drawbacks in comparison to the proposed system (Supplementary Fig. 4) that prohibit the operation in such optogenetic implants. The choice of microcontroller, its pin count, package, the integrated power management and analogue front end can be used for various tasks such as the activation of multiple μ-ILEDs and digital to analogue conversion. Two distinct classes of device, programmable intensity and multi-shank optogenetic stimulator, demonstrate some of the possibilities. Both devices represent notable advances in wireless, battery-free subdermally implanted for optogenetics.

Figure 3c summarizes a device capable of wirelessly controlling the intensity of a μ-ILED, where a sequence of images (in a clockwise direction) illustrates a demonstration program that increases the intensity. Figure 3d shows the voltage at the μ-ILEDs, where 5 Hz pulses incrementally increase in voltage, which corresponds to an increase of optical output intensity; a demonstration of this mode is also shown in Supplementary Video 1. Figure 3e highlights a spatio-optical recording of the system in a mouse home cage where the intensity is programmed to switch spatially in a way that divides the optical output in the experimental enclosure. Operation at two distinct heights in the cages (3 and 6 cm from the base) demonstrates the stability of the system regardless of spatial position in the experimental environment. This unusual capability might be useful in tuning the stimulation threshold of new opsins in vivo while observing the behaviour of the animal.

Figure 3f demonstrates capabilities in individual control of four μ-ILEDs on two bilateral probes designed for independent optogenetic stimulation/inhibition in distinct regions in the brain. This example involves a simple, sequential activation of the μ-ILEDs. Precise timing and stable, rapid turn-on behaviour of each light source is described in Fig. 3g, where each μ-ILED is set to be activated sequentially with a frequency of 1.25 Hz and a duty cycle of 10%, demonstrating independent control. Any physiologically relevant frequency, duty cycle or sequence can be programmed. Supplementary Video 2 presents various programs at frequencies visible to the naked eye, in various modes, all wirelessly activated.

The communication protocol also allows for individual addressing of multiple devices in one experimental enclosure without the need for additional hardware. Addressing of individual devices can be achieved via dedicated pulse length combinations (t_1 and t_2, Fig. 3b) for each device, complementary program state description or unique device ID. Individual addressing of the devices is demonstrated in Supplementary Video 3 where two bilateral devices are controlled individually in the same RF field,; synchronous operation as well as individual stimulation modes are shown. The addressing speed of this system depends on the LDO settling time and overall buffer capacitance in the system, ultimately limiting the number of devices that can be controlled simultaneously. Advances in addressing speed are possible via direct sensing lines that bypass the operation voltage regulation.

The power consumption of these active devices with a microcontroller, including peripherals, is summarized in Supplementary Fig. 3g where the programmable intensity device, which represents the
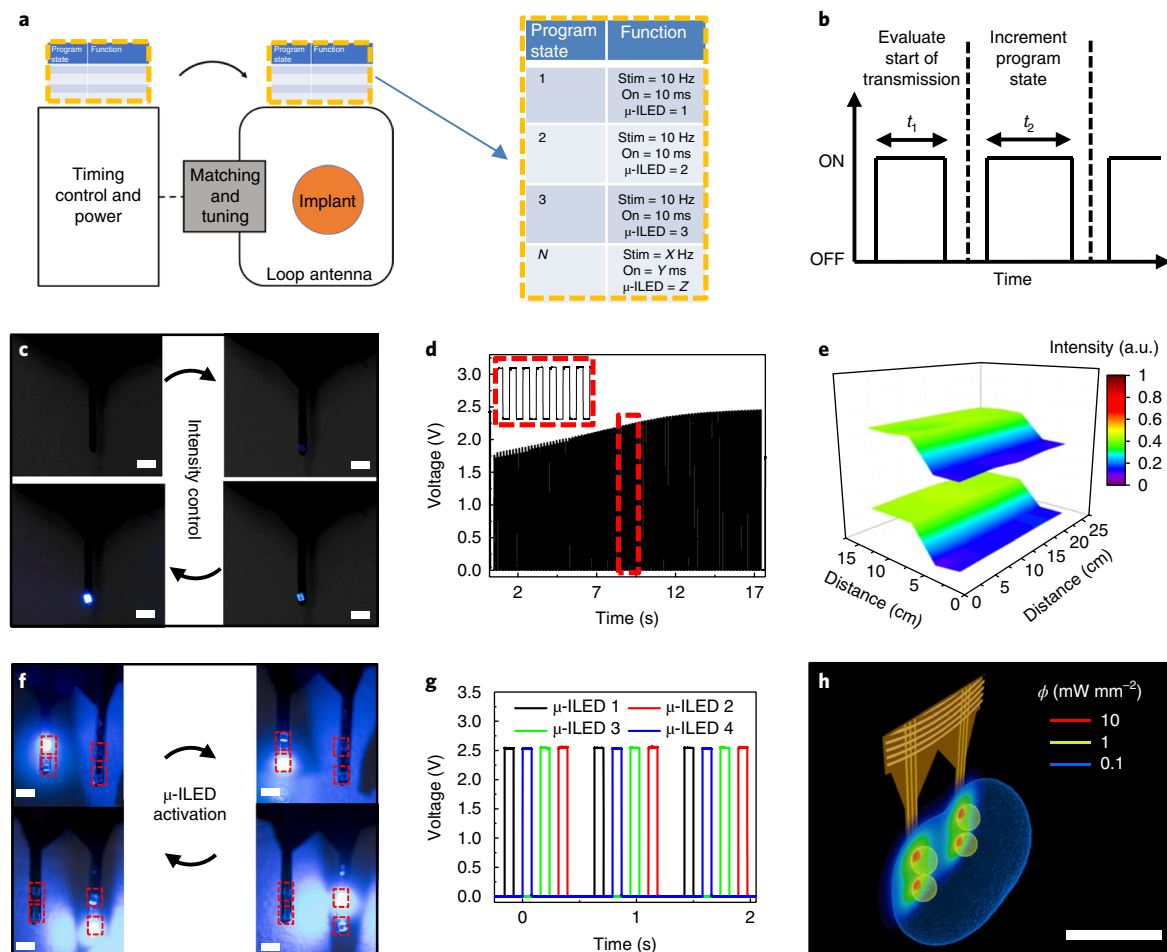
Fig. 3 | Advanced multimodal operation. a, Communication scheme for one-way communication to the implant. The inset shows an example of the non-volatile memory content of the implants. **b**, Timing diagram describing the one-way connection protocol. **c**, Images of the programmable intensity device collected during operation at increasing intensities. Scale bars, 0.5 mm. **d**, Voltage measurement at the μ-ILED during an intensity sweep at a frequency of 5 Hz, where each pulse increases in intensity. **e**, Intensity is locally controlled to enable a fixed intensity area inside a test enclosure. The mapping is repeated at 3 and 6 cm from the cage floor. **f**, Demonstration of a bilateral multi μ-ILED device with sequential activation of all stimulating μ-ILEDs. Scale bars, 0.5 mm. **g**, Corresponding voltage traces of all channels, displaying stable operation with accurate timing. **h**, 3D rendering of Monte Carlo simulations of the operation of a bilateral device at an optical emission of 10 mW mm^{-2}. Scale bar, 3 mm.

device with the greatest number of peripherals, operates at various input voltages simulating the rectified voltage in the field. Although active electronics present an overhead in power consumption, efficient energy harvesting schemes provide sufficient headroom to power devices. The optical emission profile of a bilateral device emitting at 475 nm in the brain appears in Fig. 3h, where a Monte Carlo simulation in a turbid media, replicating operation in the brain, shows the resulting local irradiance. The results show an exponential decay away from the light source, rendering an effective stimulation radius of 200–500 μm, depending on opsin efficiency, in the shape of an ellipsoid based on an input power of 10 mW mm^{-2}. Detailed slice information can be found in Supplementary Fig. 5a–e). The activation distance can be extended or decreased by modulating the input power. Detailed information on the distance dependence of the irradiance is given in Supplementary Fig. 5f. The resulting irradiance available at the implants exceeds the activation threshold of most known opsins and halerodopsins[12], and are therefore suitable for broad use for optogenetic activation and inhibition.

Capabilities in 3D imaging and chronically stable operation

The procedure for implanting the devices uses a simple stereotactic surgery that involves opening the scalp, drilling of the skull, and positioning the probe, a procedure that does not take more time or skill than an implantation of a fibre optic cannula, making this technology exceptionally easy to adapt without extra training. Although the general steps follow those in Shin et al.[7], the specifics for the bilateral, multi-μ-ILED device appear explicitly in Fig. 4 as a visual guide for implantation of such devices. In particular, Fig. 4a–e shows positioning of the device at the desired region, opening the skull to facilitate access to the brain, lowering the probe into the brain, fixing the device with cyanoacrylate glue or dental cement to restrict movement of the probes in the brain, release of the device from the stereotactic arm and bending the probe, fixing onto the skull with cyanoacrylate glue and, finally, closing the skin via suturing, a well-adapted procedure for most neuroscience researchers. Figure 4f shows an animal two weeks after surgery, highlighting minimal scarring and rapid recovery. The weight of the animals increases postoperatively up to 216 days, as evidence of their healthy status (Supplementary Fig. 6). Evaluations of device function after implantation and imaging indicate stable operation over extended periods of time, with devices still functional at the time of manuscript submission (six to nine months after implantation); Supplementary Video 4 shows the animal two weeks after surgery with an activated device (stimulation frequency 30 Hz, 20% duty-cycle) in a
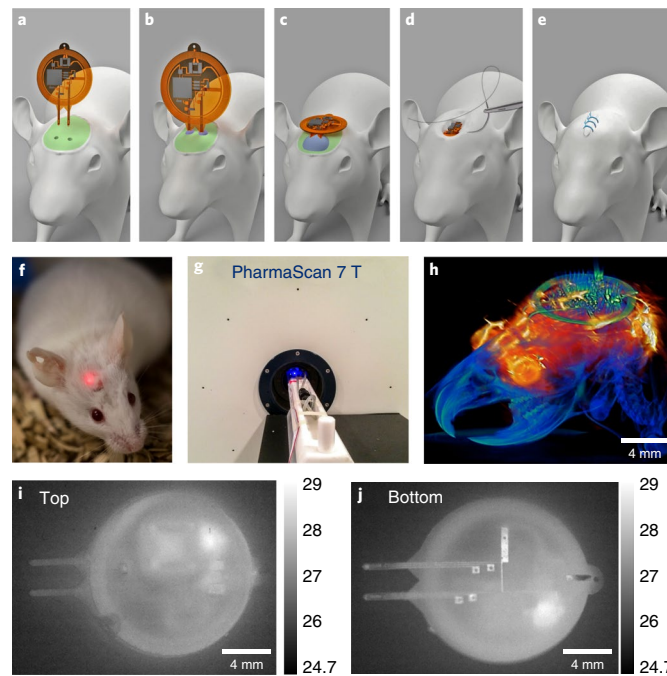
Fig. 4 | Implantation and operational capabilities. a–e, Step-by-step surgical procedure for the implantation of the programmable bilateral multi μ-ILED device. Green coloured sections indicate the skull and blue coloured sections indicate cyanoacrylate and dental cement glue. **f**, Photograph of a mouse two weeks after surgery. **g**, Implant operating in an MRI scanner. **h**, Combined image analysis with MRI and CT results superimposed in a 3D rendering of the animal implanted with the programmable bilateral multi μ-ILED device. **i**, Thermal image of the top of an operating bilateral device set to 25% duty cycle on all four μ-ILEDs. **j**, Thermal image of the bottom of an operating bilateral device set to 25% duty cycle on all four μ-ILEDs.

home cage. Materials and encapsulation schemes follow the work in Shin et al.[7], where device operation has been observed for more than 1.5 years. Additional investigations examine the immunoreactive glial responses and lesions to the brain tissue associated with the probes. Studies include animals with probes implanted for more than 200 days, as analysed with immunohistochemistry. Details are given in the Methods, with results in Supplementary Fig. 7a. Scarring to the brain tissue is less than that associated with optical fibres, and immunoreactive glial responses are similar[7]. The programmable intensity device involves similar surgical procedures, as shown in Supplementary Fig. 8. Furthermore, animals are minimally impaired by the weight of the devices (~15 mg for the regulated, 60 mg for the bilateral and 75 mg for the adjustable intensity devices, respectively). The lightweight nature is shown graphically with an image of a device floating on an aqueous foam (Supplementary Fig. 3k).

All the devices reported here are compatible with advanced imaging technologies. We demonstrate operation of the implant in a magnetic resonance imager, shown in Fig. 4g and with additional detail in Supplementary Fig. 9. Here, we examine implanted animals with a combination of computer tomography (CT) and magnetic resonance imaging (MRI) to examine the spatial location of the implanted electronics and the probe, as well as the state of the surrounding tissue. Figure 4h shows a combined image that overlays MRI slices with the 3D CT reconstruction, the superposed 3D MRI and CT images are automatically colorized highlighting the structure implant tissue and bone. Such images can also reveal details associated with the positioning and the artefact. The time requirements for the imaging procedure are also minimal, on the order of half an hour per animal, which makes this a valid tool for postoperative animal control.

Studies of the thermal load during chronic operation of the devices are summarized in Fig. 4i,j. Here, a bilateral device set to sequential, continuous operation results in a 25% duty cycle per μ-ILED, in air, and induces maximum changes in temperature that are less than 1 °C. Detailed investigations as a function of duty cycle are in Supplementary Fig. 10a,b, and were performed with the implant (regulated device) in air, which has a thermal conductivity that is an order of magnitude lower than brain tissue. This measurement set-up amplifies the effects of thermal load at high powers (4 mW electrical power) to elevate the changes in temperature to levels above the noise of the measuring equipment. Even in this scenario the tip does not heat above 1.2 °C at biologically relevant duty cycles of 40% and below. Images from an infrared camera for the case of the bilateral device reveal increases in temperature that are well below 1 °C, just above the detection threshold of the camera at the locations of the μ-ILEDs. A slight increase in temperature appears at the regulator (~1 °C), a part of the device that is located outside of the skull. Tests in realistic environments, mimicked on the bench with hydrogel (Supplementary Fig. 10c), also indicate no noticeable increases in temperature at the μ-ILED sites and only slight amounts (~1 °C) at the regulator. These data suggest safe operation in animals indefinitely, consistent with previously reported conclusions for passive devices[7,19,20].

Finite-element analysis provides further insights into the distributions of temperature that result from operation of the μ-ILEDs. For these calculations, the μ-ILEDs act as heaters operating at thermal powers that correspond, via the efficiencies of the devices, to specified irradiance levels determined by Monte Carlo simulations. The modelling focuses on the bilateral multi μ-ILED device (layouts in Supplementary Figs. 1b and 11a) because this platform presents the most challenging case of thermal load due to its use of four μ-ILEDs in close spatial proximity. The results (Supplementary Fig. 11) reveal that, for operating conditions typical of those used in optogenetic stimulation, the maximum change in temperature of the brain tissue remains below 0.4 °C. Specifically, with an activation pattern similar to that in Fig. 3g, and a thermal power of 4 mW per μ-ILED, which corresponds to an irradiance of 15.15 mW mm⁻², sufficient to activate the most common opsins (Supplementary Fig. 11b),
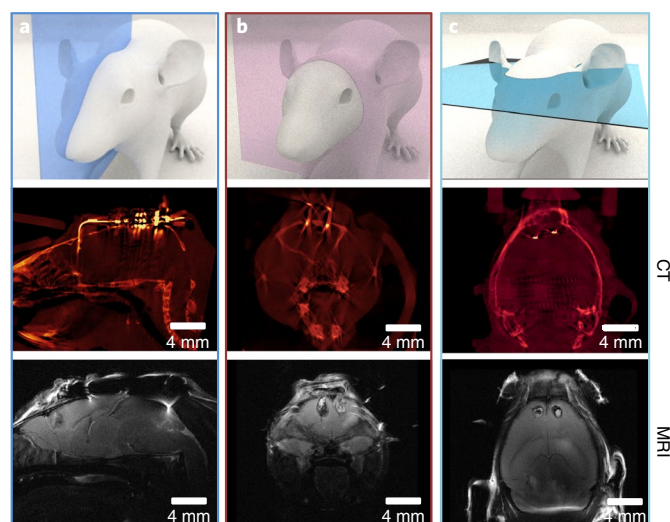
Fig. 5 | MRI and CT imaging results of the bilateral multi µ-ILED device. **a**, Sagittal orientation. **b**, Axial orientation. **c**, Coronal orientation.

the maximum change in temperature is less than 0.4 °C, a steady-state value that is reached after a few seconds of operation.

The models can also be used to explore a broader space of parameters for optogenetic stimulation, as defined in Supplementary Fig. 11i,j. At 20 Hz in a sequential pulsed mode (Supplementary Fig. 11b) irradiances of almost 40 mW mm^{-2} can be achieved (duty cycle of 10% for each µ-ILED and thermal input 9 mW, corresponding to 9.9 mW electrical input) while maintaining the maximum increase in temperature of the brain tissue below 0.5 °C (Supplementary Fig. 11i). Higher stimulation frequencies generally reduce the thermal load on the surrounding tissue.

Figure 5 shows in detail results collected from a female mouse implanted with the bilateral multi-µ-ILEDs device described above, while under light anaesthesia (isoflurane/oxygen mixture). The animal was placed on a heated bed and rectal temperature as well as breathing frequency was monitored during the imaging sessions. The safety of the implants was tested before the animal sessions and an infrared camera analysis (Supplementary Fig. 12) of the implant and surrounding tissue during extended MRI image sessions was conducted, with no noticeable heating or disruption of implant function being observed.

The resulting slice images in the sagittal, coronal and axial orientations are shown in Fig. 5a–c, with minimal post processing. The contrast of bone and dense objects for CT and the contrast of tissue for MRI yields complementary information. As expected, the implant causes some imaging artefacts in the CT reconstruction and in MRI, largely due to the semiconductor device components; counterintuitively, few artefacts are observed at the copper traces, including the antenna. Specifically, shadowing effects appear in the CT images, especially in the axial slices. The overall image quality, however, is sufficient to locate devices and their position with respect to the skull and other anatomical features. The MRI images show a surprisingly low amount of artefacts, with only slight distortions and loss of contrast around the components. Most the brain tissue is unaffected. Imaging of the power-regulated device yields similar results, as shown in Supplementary Figs. 13 and 14. In general, the quality of the CT and MRI images enables useful insights into the location of the implants and the state of bone and tissue in the animal. Future imaging that is conducted in conjunction with optogenetic stimulus is feasible, include operation inside an MRI system, as shown in Fig. 4g, Supplementary Fig. 9 and Supplementary Video 5.

Conclusions

We have reported a range of fully implantable, wireless tools for programmable, multimodal optogenetics that can address many needs in neuroscience research. The battery-free, magnetic resonant coupled operation allows for indefinite experimentation on animals that are completely free of physical or inertial motion constraints. Specifically, closed-loop feedback over the emission intensity and a power-efficient, one-way communication protocol enable user-defined, real-time control over essential operational parameters. At the same time, our approach offers effective capabilities in energy harvesting, regardless of spatial and angular position relative to the experimental housing, and can thus maintain adequate optical power levels for successful optogenetic stimulation even in large experimental environments. These tools not only facilitate standard optogenetic experimental studies, but also create new opportunities in freely moving animals.

For example, they could be used for bilateral optogenetic stimulation with individual control over neuronal populations, social experiments with individually stimulated subjects, and in vivo, rapid characterization of new opsins via precise control over emission intensity.

Methods

Device fabrication. Pyralux AP8535R served as a substrate for the flex circuit. The top and bottom copper layers (17.5 µm thick) were structured via direct laser ablation (LPKF U4). Through hole plating via pulsed direct current electroplating of copper (LPKF Contac S4) defined the electrical connections between the top and bottom layers. Components with commercial packaging were attached via reflow soldering with low-temperature solder (IndiumCorp). The µ-ILEDs were mounted with a pick-and-place tool (Finetech Fineplacer pico ma) using defined force and temperature (180 °C) with an anisotropic conductive paste. The devices were encapsulated with coatings of parylene formed by chemical vapour deposition (14 µm). Commercially packaged components such as the microcontroller and operational amplifiers were further encapsulated with polydimethylsiloxane (PDMS, Dow Corning Sylgard 184) to minimize any foreign body response.

Electronic components. Small outline, packaged off-the-shelf components served as the basis for the circuits. A low-power microcontroller (ATtiny 84 (Atmel)) with wide operational voltage capabilities provides current to the LEDs. The microcontroller firmware is programmed before device assembly. A low-dropout (150 mV), low-quiescent-current (18 µA) linear regulator with fixed internal output voltage (2.8 V) manages power to the implants (ON semiconductor NCP161). The operational amplifier for the programmable output voltage device occupies minimal space (WLCSP 1 mm × 1.5 mm) and consumes minimal power (10 µA). Passive components with 0201 and 0402 package size help to minimize the footprint.

Electromagnetic simulations. The finite-element method was adopted in the electromagnetic simulations to determine the magnetic field and the distribution of output voltage from the unregulated device in the multiplexed cage. The simulations used the commercial software Ansys HFSS (Ansys HFSS 13) with tetrahedral elements and adaptive meshing. The default adaptive convergence condition, together with a spherical surface (1,000 mm in radius) as the radiation boundary, ensured computational accuracy.

Surgical procedure. The Institutional Animal Care and Use Committee (IACUC) reviewed and approved protocols for Northwestern University's programme for the humane care and use of animals and inspects the animal facilities and investigator laboratories. Evaluation of the implanted devices was performed in compliance with Animal Welfare and Northwestern's IACUC regulations under approved IACUC protocol IS00005877 'Evaluation of biocompatible devices in vivo model'. The animal study was conducted in 20–27gram CD1 IGS mice (Crl: CD1(ICR)). The sterilized device was sterotactically implanted into the right striatum of anaesthetized mice. Coordinates are referenced from bregma: 0 mm antero-posterior, +2.5 mm medio-lateral and ±1 mm medio-lateral (for the bilateral device). The animals were checked daily for distress, pain and moribund condition.

Optical intensity distribution calculation. Monte Carlo simulations[21,22] were carried out to simulate the illumination pattern of the bilateral device set in turbid media replicating operational conditions in the brain. The simulation volume consisted of a rectangular grid with 5,003 bins with 25 µm bin size. A total of 7.85 × 10^6 photons was launched from a rectangular source (µ-ILED footprint 0.22 mm × 0.27 mm) with 120° full divergence angle. Photon propagation was performed in brain matter with a 0.6 cm^{-1} absorption coefficient[23], 211 cm^{-1} scattering coefficient and 0.86 anisotropy factor[24]. The spatial distribution of the photon fluence rate (ϕ [mm^{-2}]) was extracted and normalized with respect to the illumination irradiance of one individual µ-ILED source (10 mW mm^{-2}).

Thermal finite-element analysis model. Finite-element modelling was implemented with the commercial software ABAQUS (ABAQUS Analysis User's Manual 2010, V6.10) to study the changes in temperature of brain tissue that is in direct contact the μ-ILED equipped probes. Components of the probe in their actual layouts, including all layers of encapsulation and associated topology were simulated. The tissue and μ-ILEDs were modelled by hexahedral elements (DC3D8), the minimal mesh size was less than 1/10th of the thickness (4 μm) of the μ-ILEDs, with at least three mesh elements for the thinnest layers, such as the parylene encapsulation; the mesh convergence of the simulation was ensured. The thermal conductivity, heat capacity and mass density used in the simulations was $0.5\,W\,m^{-1}\,K^{-1}$, $3,700\,J\,kg^{-1}\,K^{-1}$ and $1,050\,kg\,m^{-3}$ for the brain tissue; $130\,W\,m^{-1}\,K^{-1}$, $490\,J\,kg^{-1}\,K^{-1}$ and $6,150\,kg\,m^{-3}$ for the μ-ILEDs; $377\,W\,m^{-1}\,K^{-1}$, $386\,J\,kg^{-1}\,K^{-1}$ and $8,920\,kg\,m^{-3}$ for the Cu traces; $0.15\,W\,m^{-1}\,K^{-1}$, $1,510\,J\,kg^{-1}\,K^{-1}$ and $1,000\,kg\,m^{-3}$ for the PDMS encapsulation; $0.21\,W\,m^{-1}\,K^{-1}$, $2,100\,J\,kg^{-1}\,K^{-1}$ and $909\,kg\,m^{-3}$ for the PI; $0.126\,W\,m^{-1}\,K^{-1}$, $837\,J\,kg^{-1}\,K^{-1}$ and $1,110\,kg\,m^{-3}$ for the parylene encapsulation.

MicroCT imaging. Respiratory signals were monitored using a digital system developed by Mediso (Mediso-USA). Images were acquired with a preclinical microPET/CT imaging system,(Mediso nanoScan scanner). Data were acquired with 'medium' magnification, 33 μm focal spot, 1 × 1 binning, with 720 projection views over a full circle, with a 300 ms exposure time. Three images were acquired, using 35 kVp, 50 kVp and 70 kVp (where kVp is peak kilovoltage). The projection data was reconstructed with a voxel size of 68 μm using filtered (Butterworth filter) back-projection software from Mediso.

MRI imaging. MRI was performed on a 9.4 T Bruker Biospec MRI system with a 30 cm bore, a 12 cm gradient insert, and an Autopac automated sample positioning system (Bruker Biospin Inc.). Respiratory signals were monitored using an MR-compatible physiologic monitoring system (SA Instruments) and a warm-water circulating system was used to maintain body temperature. An actively decoupled four-channel phased array receive-only radiofrequency coil designed for mouse brain (Bruker Biospin, Inc.) was mounted on the bed. This assembly was centred inside a 72 mm quadrature volume coil in transmit-only mode (Bruker Biospin, Inc.). Mice were imaged using an accelerated spin echo sequence (Rapid Acquisition with Relaxation Enhancement, RARE) oriented in the axial, sagittal and coronal directions. The following parameters were used: TR/TE = 2,000 ms / 40 ms, RARE factor 8, MTX = 256 × 256, FOV 2 × 2 cm, 11–17 slices of 0.75–1 mm thick (as needed for full brain coverage), and 2 signal averages. Fat saturation was disabled as this was found to slightly reduce image artefacts from the implanted devices. Acquisition time was approximately 2 min per scan. The reconstructed data were visualized in Amira 6.4 (FEI). MRI and microCT images were manually registered, as the image artefacts caused by the device precluded automatic image registration. A non-local means filter was applied to the CT data in Amira to reduce image artefacts.

Operational tests of the battery-free wireless implant were performed in a 7 T Bruker PharmaScan system.

Immunohistochemistry. Procedures for immunohistochemistry follow protocols described in ref. [19]. Mice were anaesthetized with isofluorane and intracardially perfused with ice cold phosphate buffer saline (PBS) and 4% paraformaldehyde in PBS. Brains were dissected, postfixed for 24 h at 4 °C, and cryoprotected with a solution of 30% sucrose in 0.1 M phosphate buffer (pH 7.4) at 4 °C for at least 24 h. Brains were then cut into 30-μm sections on a VT1200 S Vibrating-blade microtome. Thirty-micrometre brain sections were washed two or three times in PBS and blocked in blocking buffer (PBS containing 0.5% Triton X-100 and 5% normal goat serum) for 1 h. Sections were then incubated for ~16 h at 4 °C in blocking buffer containing guinea pig anti-GFAP (1:500) and rabbit anti-Iba1 (1:300). Following incubation, sections were washed three times in PBS and then incubated for 2 h at room temperature in blocking buffer containing Alexa Fluor 488 goat anti-rabbit IgG (1:1,000), Alexa Fluor 568 goat anti-guinea pig IgG (1:1,000), and Neurotrace 435/455 Blue Fluorescent Nissl stain (1:100). Following the secondary antibody, sections were washed three times in PBS and then mounted on glass slides with hardset Vectashield (Vector Labs). All sections were imaged on a Leica SP8 confocal microscope. Gain, exposure time, and z-stack size remained constant throughout each experiment. All images were processed with the same settings by using Fiji ImageJ.

Reporting Summary. Further information on research design is available in the Nature Research Reporting Summary linked to this article.

Data availability

The data that support the plots within this paper and other findings of this study are available from the corresponding author upon reasonable request.

References

1. Boyden, E. S., Zhang, F., Bamberg, E., Nagel, G. & Deisseroth, K. Millisecond-timescale, genetically targeted optical control of neural activity. *Nat. Neurosci.* **8**, 1263–1268 (2005).
2. Deisseroth, K. Optogenetics. *Nat. Methods* **8**, 26–29 (2011).
3. Park, S. I. et al. Soft, stretchable, fully implantable miniaturized optoelectronic systems for wireless optogenetics. *Nat. Biotechnol.* **33**, 1280–1286 (2015).
4. Pisanello, F. et al. Multipoint-emitting optical fibers for spatially addressable in vivo optogenetics. *Neuron* **82**, 1245–1254 (2014).
5. Yizhar, O., Fenno, L. E., Davidson, T. J., Mogri, M. & Deisseroth, K. Optogenetics in neural systems. *Neuron* **71**, 9–34 (2011).
6. Chen, R., Canales, A. & Anikeeva, P. Neural recording and modulation technologies. *Nat. Rev. Mater.* **2**, 16093 (2017).
7. Shin, G. et al. Flexible near-field wireless optoelectronics as subdermal implants for broad applications in optogenetics. *Neuron* **93**, 509–521 (2017). e503.
8. Montgomery, K. L. et al. Wirelessly powered, fully internal optogenetics for brain, spinal and peripheral circuits in mice. *Nat. Methods* **12**, 969–974 (2015).
9. Park, S. I. et al. Stretchable multichannel antennas in soft wireless optoelectronic implants for optogenetics. *Proc. Natl Acad. Sci. USA* **113**, E8169–E8177 (2016).
10. Ho, J. S. et al. Self-tracking energy transfer for neural stimulation in untethered mice. *Phys. Rev. Appl.* **4**, 024001 (2015).
11. Gutruf, P. & Rogers, J. A. Implantable, wireless device platforms for neuroscience research. *Curr. Opin. Neurobiol.* **50**, 42–49 (2018).
12. Klapoetke, N. C. et al. Independent optical excitation of distinct neural populations. *Nat. Methods* **11**, 338–346 (2014).
13. Akerboom, J. et al. Genetically encoded calcium indicators for multi-color neural activity imaging and combination with optogenetics. *Front. Mol. Neurosci.* https://doi.org/10.3389/fnmol.2013.00002 (2013).
14. Harvey, C. D., Collman, F., Dombeck, D. A. & Tank, D. W. Intracellular dynamics of hippocampal place cells during virtual navigation. *Nature* **461**, 941–946 (2009).
15. Tye, K. M. et al. Amygdala circuitry mediating reversible and bidirectional control of anxiety. *Nature* **471**, 358–362 (2011).
16. Hight, A. E. et al. Superior temporal resolution of Chronos versus channelrhodopsin-2 in an optogenetic model of the auditory brainstem implant. *Hear. Res.* **322**, 235–241 (2015).
17. Gerlai, R. A small fish with a big future: zebrafish in behavioral neuroscience. *Rev. Neurosci.* **22**, 3–4 (2011).
18. Yartsev, M. M. & Ulanovsky, N. Representation of three-dimensional space in the hippocampus of flying bats. *Science* **340**, 367–372 (2013).
19. Lu, L. et al. Wireless optoelectronic photometers for monitoring neuronal dynamics in the deep brain. *Proc. Natl Acad. Sci. USA* **115**, E1374–E1383 (2018).
20. Samineni, V. K. et al. Fully implantable, battery-free wireless optoelectronic devices for spinal optogenetics. *Pain* **158**, 2108–2116 (2017).
21. Wang, L., Jacques, S. L. & Zheng, L. MCML—Monte Carlo modeling of light transport in multi-layered tissues. *Comput. Methods Programs Biomed.* **47**, 131–146 (1995).
22. Keijzer, M., Jacques, S. L., Prahl, S. A. & Welch, A. J. Light distributions in artery tissue: Monte Carlo simulations for finite-diameter laser beams. *Lasers Surg. Med.* **9**, 148–154 (1989).
23. Yaroslavsky, A. et al. Optical properties of selected native and coagulated human brain tissues in vitro in the visible and near infrared spectral range. *Phys. Med. Biol.* **47**, 2059 (2002).
24. Yona, G., Meitav, N., Kahn, I. & Shoham, S. Realistic numerical and analytical modeling of light scattering in brain tissue for optogenetic applications. *eNeuro* **3**, ENEURO.0059-0015.2015 (2016).

Acknowledgements

Author contributions

P.G., A.V.-G., Z.X. and J.A.R. designed research. P.G., V.K., A.V.-G., Z.X., A.B., C.-J.S., Y.X., C.R.H., E.A.W., I.K., S.R.K, T.R. and J.P.L. performed research. P.G., A.V.-G., Z.X., C.R.H., E.A.W., I.K., Y.H., D.C. and J.A.R. analysed data. P.G. and J.A.R. wrote the paper.

Additional information

nature research

Corresponding author(s):

Double-blind peer review submissions: write DBPR and your manuscript number here instead of author names.

John A. Rogers
11/14/2017

Reporting Summary

Nature Research wishes to improve the reproducibility of the work that we publish. This form provides structure for consistency and transparency in reporting. For further information on Nature Research policies, see Authors & Referees and the Editorial Policy Checklist.

Statistical parameters

When statistical analyses are reported, confirm that the following items are present in the relevant location (e.g. figure legend, table legend, main text, or Methods section).

n/a	Confirmed	
☐	☒	The exact sample size (*n*) for each experimental group/condition, given as a discrete number and unit of measurement
☐	☒	An indication of whether measurements were taken from distinct samples or whether the same sample was measured repeatedly
☒	☐	The statistical test(s) used AND whether they are one- or two-sided *Only common tests should be described solely by name; describe more complex techniques in the Methods section.*
☒	☐	A description of all covariates tested
☐	☒	A description of any assumptions or corrections, such as tests of normality and adjustment for multiple comparisons
☒	☐	A full description of the statistics including central tendency (e.g. means) or other basic estimates (e.g. regression coefficient) AND variation (e.g. standard deviation) or associated estimates of uncertainty (e.g. confidence intervals)
☒	☐	For null hypothesis testing, the test statistic (e.g. *F*, *t*, *r*) with confidence intervals, effect sizes, degrees of freedom and *P* value noted *Give P values as exact values whenever suitable.*
☒	☐	For Bayesian analysis, information on the choice of priors and Markov chain Monte Carlo settings
☒	☐	For hierarchical and complex designs, identification of the appropriate level for tests and full reporting of outcomes
☒	☐	Estimates of effect sizes (e.g. Cohen's *d*, Pearson's *r*), indicating how they were calculated
☐	☒	Clearly defined error bars *State explicitly what error bars represent (e.g. SD, SE, CI)*

Our web collection on statistics for biologists may be useful.

Software and code

Policy information about availability of computer code

Data collection   For this study the following software was used to collect data and program devices: Mathlab, Excel, Arduino

Data analysis   Data analysis and plotting was executed with Excel and Origin

For manuscripts utilizing custom algorithms or software that are central to the research but not yet described in published literature, software must be made available to editors/reviewers upon request. We strongly encourage code deposition in a community repository (e.g. GitHub). See the Nature Research guidelines for submitting code & software for further information.

Data

Policy information about availability of data

All manuscripts must include a data availability statement. This statement should provide the following information, where applicable:

- Accession codes, unique identifiers, or web links for publicly available datasets
- A list of figures that have associated raw data
- A description of any restrictions on data availability

The data that support the plots within this paper and other findings of this study are available from the corresponding author upon reasonable request

Field-specific reporting

Please select the best fit for your research. If you are not sure, read the appropriate sections before making your selection.

☒ Life sciences   ☐ Behavioural & social sciences   ☐ Ecological, evolutionary & environmental sciences

Life sciences study design

All studies must disclose on these points even when the disclosure is negative.

Sample size	All data was reported in the manuscript. Sample size was chose according to reports available in literature
Data exclusions	No data was excluded
Replication	Multiple data points have been collected in the case of biology studies.
Randomization	N/A
Blinding	N/A

Reporting for specific materials, systems and methods

Materials & experimental systems

n/a	Involved in the study
☒	☐ Unique biological materials
☒	☐ Antibodies
☒	☐ Eukaryotic cell lines
☒	☐ Palaeontology
☐	☒ Animals and other organisms
☒	☐ Human research participants

Methods

n/a	Involved in the study
☒	☐ ChIP-seq
☒	☐ Flow cytometry
☒	☐ MRI-based neuroimaging

Animals and other organisms

Policy information about studies involving animals; ARRIVE guidelines recommended for reporting animal research

Laboratory animals	Animal study was conducted in 20—27gram CD1 IGS mice (Crl: CD1(ICR)).
Wild animals	NA
Field-collected samples	NA

John G. Rogers
11/14/2018